OXFORD

Cerebral Cortex, 2023, **33**, 9917–9926
https://doi.org/10.1093/cercor/bhad254
Advance access publication date 6 July 2023
Original Article

Velocity of conduction between columns and layers in barrel cortex reported by parvalbumin interneurons

Katherine S. Scheuer[1], John M. Judge[2], Xinyu Zhao[3,4], Meyer B. Jackson[4,*]

[1]Cellular and Molecular Biology Program, University of Wisconsin-Madison, Madison, WI 53705, United States,
[2]Biophysics Program, University of Wisconsin-Madison, Madison, WI 53705, United States,
[3]Waisman Center, University of Wisconsin-Madison, Madison, WI 53705, United States,
[4]Department of Neuroscience, University of Wisconsin-Madison, Madison, WI 53705, United States

*Corresponding author: Department of Neuroscience, University of Wisconsin-Madison, 1111 Highland Ave., Room 5505 WIMR-II, Madison, WI 53705, United States. Email: meyer.jackson@wisc.edu

Inhibitory interneurons expressing parvalbumin (PV) play critical roles throughout the brain. Their rapid spiking enables them to control circuit dynamics on a millisecond time scale, and the timing of their activation by different excitatory pathways is critical to these functions. We used a genetically encoded hybrid voltage sensor to image PV interneuron voltage changes with sub-millisecond precision in primary somatosensory barrel cortex (BC) of adult mice. Electrical stimulation evoked depolarizations with a latency that increased with distance from the stimulating electrode, allowing us to determine conduction velocity. Spread of responses between cortical layers yielded an interlaminar conduction velocity and spread within layers yielded intralaminar conduction velocities in different layers. Velocities ranged from 74 to 473 μm/ms depending on trajectory; interlaminar conduction was 71% faster than intralaminar conduction. Thus, computations within columns are more rapid than between columns. The BC integrates thalamic and intracortical input for functions such as texture discrimination and sensory tuning. Timing differences between intra- and interlaminar PV interneuron activation could impact these functions. Imaging of voltage in PV interneurons reveals differences in signaling dynamics within cortical circuitry. This approach offers a unique opportunity to investigate conduction in populations of axons based on their targeting specificity.

Key words: axonal conduction; action potential propagation velocity; inhibitory interneurons; parvalbumin; somatosensory cortex.

Introduction

Expression of the Ca^{2+}-binding protein parvalbumin (PV) defines a broad class of inhibitory interneurons that have been implicated in psychiatric and neurological disorders including schizophrenia, bipolar disorder, and autism spectrum disorder (Liu et al. 2012; Gonzalez-Burgos et al. 2015; Lauber et al. 2018). Because PV interneurons fire rapidly and have a short membrane time constant, they play a critical role in controlling the temporal integration window of their targets (Pouille and Scanziani 2001; Galarreta and Hestrin 2002; Cardin 2018; Ferguson and Gao 2018). PV interneurons are distributed throughout the cortex, including the whisker-responsive primary somatosensory cortex, or barrel cortex (BC), where their anatomy, circuitry, and function have received much attention (Staiger and Petersen 2021). BC is divided into visually distinct cytoarchitectural units, or barrels, giving the region its name (Woolsey and Van der Loos 1970). Each barrel receives input from one vibrissa. Barrel column boundaries, visible in L4, can be extended through supragranular and infragranular layers (Lefort et al. 2009; Staiger and Petersen 2021). Whisker inputs follow the canonical circuit, passing through the lemniscal pathway from the ventral posteromedial thalamus to a distinct barrel in L4 before being relayed to L2/3 and then L5. However, BC also contains a number of noncanonical pathways, including those extending between two or more columns, and receives long-range inputs from a variety of areas including multiple thalamic regions, primary motor, auditory, and visual cortices, and secondary motor and somatosensory cortices (Staiger and Petersen 2021). Functionally, BC has been implicated not only in touch and whisking (Feldmeyer 2012; Staiger and Petersen 2021) but also in sensing movement (Ayaz et al. 2019), texture discrimination (Allitt et al. 2017; Isett et al. 2018; Vecchia et al. 2020), object localization (O'Connor et al. 2010), and social interactions (Lenschow and Brecht 2015). However, many questions remain about the roles of PV interneurons in these processes.

PV interneurons are present in L2-6 in BC and participate in essentially all BC functions, enhancing spatial and temporal resolution, enforcing sparse coding, and providing both feedback and feedforward inhibition (Staiger and Petersen 2021; Yeganeh et al. 2022). PV interneurons also contribute to computations across columns and cortical layers. Excitation/inhibition balance and gamma oscillation frequency, both linked to PV interneuron function, differ between cortical layers (Xu et al. 2016; Adesnik 2018). Due to the fast-spiking nature of PV interneurons, these cells are likely to influence rapid computations. Measurement of conductance velocity in the activation of PV interneurons across cortical layers and columns will advance our understanding of the determinants of their timing and thus their roles in these computations.

Here we use the genetically encoded hybrid voltage sensor hybrid voltage sensor (hVOS) to investigate the timing of activation of PV interneurons within a column between layers (interlaminar), as well as within a layer between columns (intralaminar). Imaging reveals responses from many cells distributed through multiple cortical layers and columns with sub-millisecond

Received: May 5, 2023. **Revised:** June 21, 2023. **Accepted:** June 22, 2023
© The Author(s) 2023. Published by Oxford University Press. All rights reserved. For permissions, please e-mail: journals.permissions@oup.com

precision (Chanda et al. 2005; Wang et al. 2010; Ghitani et al. 2015). Velocities of conduction in efferents to the somatosensory cortex have been well studied (Swadlow 1990, 1991), but conduction of axons within the cortex has received less attention. By targeting hVOS probe to PV interneurons (Bayguinov et al. 2017), we were able to track the temporal spread of their activation by excitatory axons that run within and between layers. Our measurements of velocity generally fell in the range of previously reported values in cortex. We found that interlaminar conduction velocity within a column is 71% faster than intralaminar conduction velocity across columns. Thus, PV interneuron-related computations within columns can be faster than those between columns, and this is likely to have functional consequences within and beyond BC.

Materials and methods

Animals

Ai35-hVOS1.5 (C57BL/6-*Gt(ROSA)26Sor*$^{tm1(CAG\text{-}hVOS1.5)Mbja}$/J, https://www.jax.org/strain/031102) Cre reporter mice (Bayguinov et al. 2017) were bred with PV Cre driver mice (B6.129P2-Pvalb$^{tm1(cre)Arbr}$/J, https://www.jax.org/strain/017320) to create animals with PV interneuron-specific hVOS probe expression. All animal procedures were approved by the Animal Care and Use Committee of the University of Wisconsin-Madison School of Medicine and Public Health (IACUC protocol: M005952).

Hybrid voltage sensor

The hVOS probe used here harbors a cerulean fluorescent protein (CeFP) tethered to the inner face of the plasma membrane by a truncated h-ras motif (Wang et al. 2010). Slices are perfused with 4 μM dipicrylamine (DPA), a small anion that partitions into the cell membrane. Membrane depolarization drives DPA toward the CeFP to quench fluorescence through Förster resonance energy transfer, and repolarization drives the DPA away allowing fluorescence to return to baseline (Chanda et al. 2005; Wang et al. 2010). Fluorescence thus reports voltage changes selectively from PV interneurons because the PV Cre driver used here drives probe expression specifically and efficiently in these cells (Bayguinov et al. 2017). DPA has a response time <0.5 ms (Chanda et al. 2005; Bradley et al. 2009), enabling hVOS fluorescence to track action potentials in single cells with excellent temporal fidelity (Ghitani et al. 2015; Ma et al. 2019).

Slice preparation

Six- to ten-week-old male and female mice were deeply anesthetized with isoflurane and sacrificed via cervical dislocation. Brains were dissected and placed into ice-cold cutting solution (in mM: 10 glucose, 125 NaCl, 4 KCl, 1.25 NaH_2PO_4, 26 $NaHCO_3$, 6 $MgSO_4$, 1 $CaCl_2$) bubbled with 95% O_2/5% CO_2. Coronal slices (300 μm) were prepared using a Leica VT1200S vibratome and placed into artificial cerebrospinal fluid (ACSF, same as cutting solution except 1.3 mM $MgSO_4$, 2.5 mM $CaCl_2$,) and bubbled with 95% O_2/5% CO_2 for at least 1 h. ACSF used for slice storage and recording contained 4 μM DPA.

Voltage imaging

Slices were continuously perfused with ACSF at room temperature and viewed using a BX51 Olympus microscope and Olympus XLUMPlanFl 20 × objective (N.A. 1.0). Layer and barrel boundaries were visually identified in fluorescence and gradient contrast images (e.g. Fig. 1A–F). Stimulus pulses (100 μA, 180-μs, except Fig. 2A–C that used 10–60 μA) were generated by triggering a stimulus isolator (World Precision Instruments, Sarasota, Florida) and applied via fire-polished, ACSF-filled KG-33 glass electrodes (King Precision Glass, Claremont, California) with tip diameter ~6–8 μm. Stimulus electrodes were positioned in various locations within BC with a micromanipulator. Displayed traces of fluorescence versus time were averages of five trials, at 15 s intervals. Slices were illuminated with an light emitting diode (LED) light source (Prizmatix, Holon, Israel) with peak emission at 435 nm. Gradient contrast images were acquired with a high-resolution Kiralux CMOS camera (Thorlabs, Newton, New Jersey); fluorescence images were acquired with this camera for better visualization, but for voltage imaging we used a CCD-SMQ camera (RedShirt Imaging, Decatur, Georgia) at a framerate of 2,000 Hz and 80 × 80 spatial resolution. A movable mirror within a dual-port adapter was used to switch between cameras while an experiment was underway without mechanical disturbance. Imaging was controlled with a custom acquisition and analysis program that gates stimulation and illumination (Chang 2006).

Data processing, analysis, and velocity determination

Fluorescence divided by resting light intensity (ΔF/F) was passed through a nine-point binomial temporal filter and a spatial filter with $\sigma = 1$. A polynomial baseline correction was calculated using fluorescence outside of a 20 ms measurement window from 4 ms before to 16 ms after the stimulus. Signal-to-noise ratio (SNR) was calculated as the maximum amplitude divided by the standard deviation of noise in a 50-ms prestimulus window.

Signals in PV interneurons were used to track propagation through columns and layers by selecting contiguous groups of pixels as regions of interest (ROIs). A sequence of ROIs ~20 μm thick was drawn using an automated procedure along the hypothesized direction of propagation, with widths spanning the barrel (illustrated in Fig. 3C). To ensure accuracy, only ROIs where the traces had SNR >5 were included. Propagation distances used in the interlaminar velocity calculations were the distances from the stimulation site to each ROI center along the propagation trajectory parallel to the column edges. An analogous process was employed for intralaminar velocities between columns and within layers. Within each ROI, traces of fluorescence versus time were averaged and used to determine latency, defined as the time from stimulation to half-maximal response (illustration in Fig. 3D). The average root-mean-square error of the latencies used in this study was 0.214 ms. Based on the number of pixels with SNR >5 and the size of a PV interneuron, we estimate an ROI contains 2–15 responsive cells. Because ROIs contain multiple cells, response half-widths broaden with distance from the electrode as activation becomes less synchronous. This has also observed in hVOS imaging experiments of action potential propagation in populations of axons (Ma et al. 2017).

In addition to monosynaptic responses, stimulation often evoked disynaptic components and direct responses to electrical stimulation. Direct responses were generally insensitive to glutamate receptor blockade (Canales et al. 2022), were confined to within 45 μm of the tip of the stimulating electrode and had latencies <1 ms after stimulation. Direct and disynaptic responses identified using sequences of SNR heatmaps and traces of fluorescence versus time (Fig. S1, Supplemental Material) were excluded from analysis. Monosynaptic responses exhibited a clear wavelike pattern of spread with a velocity that was readily measured from the slope of the observed spread. Conduction velocity was calculated as the inverse of the slope from fits by linear regression to plots of distance versus latency (illustrated

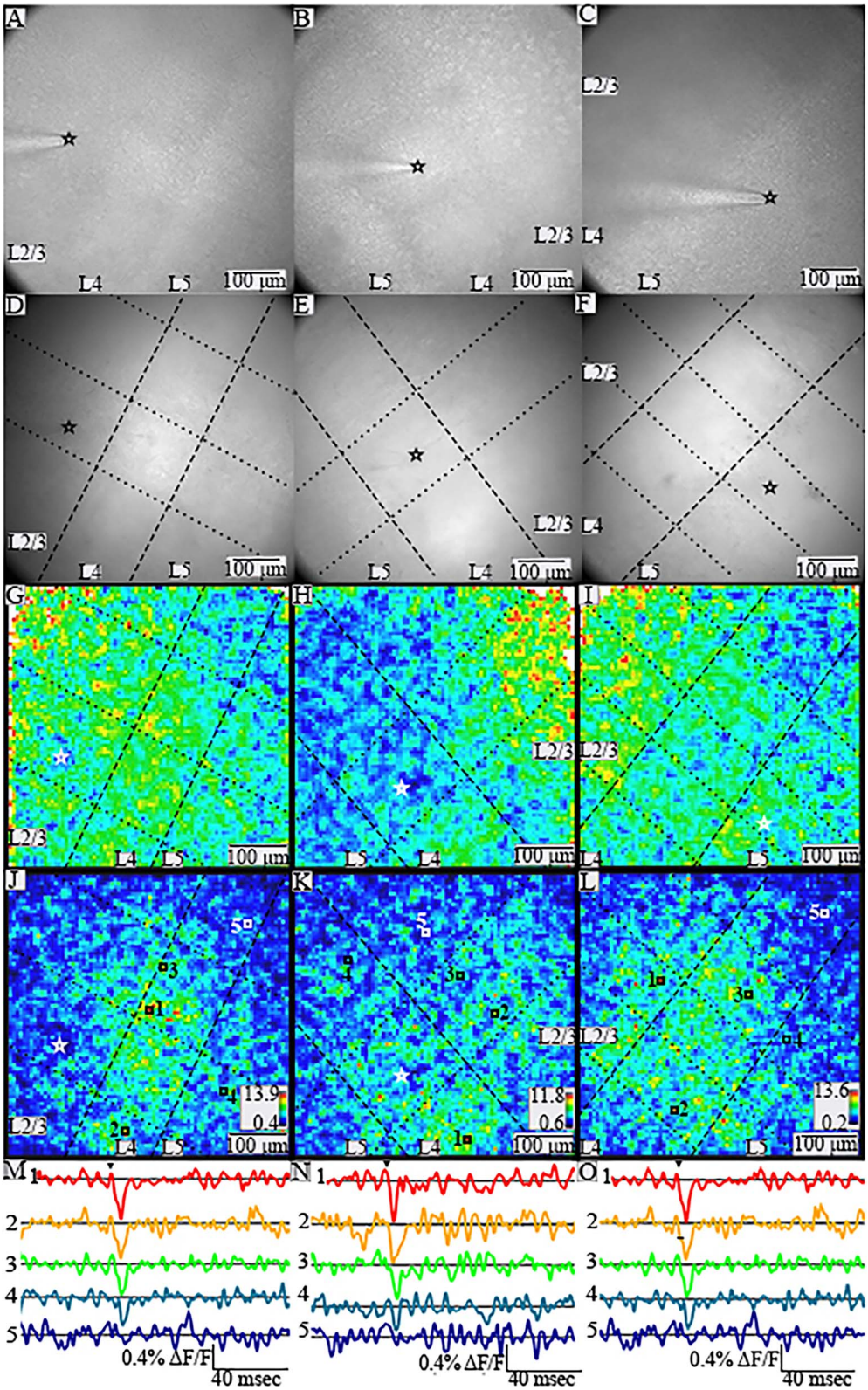

Fig. 1. PV interneurons throughout a slice respond with different spatial patterns to stimulation in different layers. (A)–(C). Gradient contrast images of slices of BC, all with L2/3 through L5 within the field of view. The tip of the stimulating electrode is visible in L2/3 (A), L4 (B), and L5 (C), and its position is indicated by black or white stars in panels A–L. (D)–(F). Fluorescence images for the same slices in A–C. In (D)–(L) dashed lines show layer boundaries, and dotted lines show column boundaries. (G)–(I) Heatmaps of maximum amplitude in 20-ms windows for the corresponding slices above. Warmer colors correspond to larger peak amplitudes. A few white pixels at the edges reflect saturation due to higher noise with lower light levels. (J)–(L) SNR heatmaps for the corresponding slices above. Both maximum amplitude and SNR heatmaps are based on images acquired using different cameras than for gradient contrast and fluorescent images, so the fields of view do not align precisely. Warmer colors indicate higher SNR (scales and ranges indicated in lower right corners). Locations with higher SNR have stimulus-evoked responses in selected traces of fluorescence versus time (M)–(O) from numbered locations (indicated with white or black squares) in the corresponding SNR heatmaps above. Arrowheads above top traces indicate time of stimulation.

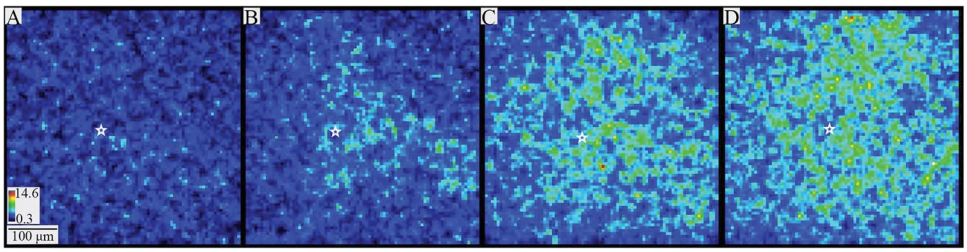

Fig. 2. PV interneuron responses to different stimulation currents. Heatmaps of SNR in 20-ms windows following 10 μA (A), 20 μA (B), 60 μA (C), and 100 μA (D) stimulation. As current intensity increases, responses are visible through progressively larger areas. The stimulation site is marked with a white star in each panel. Heatmap scale in A also applies to B–D.

in Fig. 3F). Plots had at least seven points, and *P*-values were corrected for multiple tests using the false discovery rate.

Analysis included 31 slices from 13 animals (six male and seven female). To determine the appropriate statistical tests, normality was evaluated with Shapiro–Wilk tests ("stats" package in R), and differences in group variances were evaluated with Levene's tests ("car" package in R). Conduction velocity was normally distributed ($W = 0.940$, $P = 0.084$). Variance did not differ significantly for male and female animals [$F(1, 29) = 0.001$, $P = 0.974$] or for inter- and intralaminar velocities [$F(1, 29) = 1.721$, $P = 0.200$]. It also did not differ for interlaminar conduction velocity from L2/3 to L4 and L5 (L2/3 → L5), interlaminar conduction velocity from L4 to L2/3 (L4 → L2/3) or L4 to L5 (L4 → L5), interlaminar conduction velocity from L5 to L2/3 or L4 (L5 → L2/3), intralaminar L2/3 conduction velocity, or intralaminar L4 conduction velocity [$F(4, 26) = 1.437$, $P = 0.250$]. Interlaminar versus intralaminar velocities, and velocities for male versus female animals were compared with *t*-tests. Conduction velocity for different trajectories was compared with ANOVA. Conduction velocity did not differ significantly between sexes [$t(28.898) = -1.437$, $P = 0.161$].

Custom software, Python code (used to draw ROIs automatically), and R code (used for statistical analysis) are available on request. Data from displayed figures will be made available in response to reasonable requests.

Results

PV interneuron responses to stimulation in L2/3, L4, and L5

We crossed PV-Cre driver mice with hVOS-Cre reporter mice to generate double transgenic PV-Cre;hVOS mice. We have previously shown that in the brain of PV-Cre;hVOS mice, hVOS probe is expressed in 83% of PV interneurons with 99.2% specificity (Bayguinov et al. 2017). Figure 1A–C presents gradient contrast images of three BC slices from PV-Cre;hVOS mice, and Fig. 1D–F presents the fluorescence images of these slices (note that the images were taken with different cameras, so the fields of view do not align precisely). Cortical layers were identified by cell density and cell size (Woolsey and Van der Loos 1970; Feldmeyer 2012) using both gradient contrast (Fig. 1A–C) and fluorescence (Fig. 1D–F). The boundaries between layers are marked with dashed lines (Fig. 1D–L), and fields of view generally contained L2/3 through L5. We also identified barrels, which are separated by faint "hollows" (Woolsey and Van der Loos 1970; Feldmeyer 2012) as well as stronger fluorescence in L4. Boundaries between barrel columns are marked by dotted lines (Fig. 1D–L). We assessed the velocity of spread of PV interneuron responses following stimulation in L2/3, L4, and L5. This elicited fluorescence changes associated with the depolarization of PV interneurons. Responses were seen throughout the field of view, and the distributions of peaks within a 20 ms window are illustrated in amplitude (Fig. 1G–I) and SNR heatmaps (Fig. 1J–L). Warmer colors correspond to larger depolarizations. Compared to the SNR heatmaps, amplitude heatmaps are less clear due to spatial variations in noise level within the field of view. Low levels of light in the weakly illuminated periphery of the field of view (for example, ROI 21 in Fig. 3C and E), lead to high noise levels and artificially elevated ΔF/F values that obscure spatial response patterns in the rest of the slice. We therefore used SNR heatmaps for visualizing spread. Traces of fluorescence versus time from different locations (indicated by number and color) reveal corresponding variations in the magnitude of stimulus-evoked PV interneuron depolarization, where fluorescence decreases as voltage drives DPA toward the fluorescent protein of the hVOS probe (Fig. 1M–O). Dark blue regions of the heatmaps indicate the absence of PV interneurons with responses above our detection threshold, and traces from those locations show no discernable stimulus-evoked fluorescence changes (traces 5 in Fig. 1M–O).

Increasing the stimulation current elicited responses in more cells over greater distances. SNR heatmaps reflecting responses within a 20-ms window around the stimulation time (Fig. 2) revealed that 10 μA stimulation rarely elicited detectable responses (Fig. 2A). Increasing the stimulus current to 20 μA (Fig. 2B), 60 μA (Fig. 2C), and 100 μA (Fig. 2D) depolarized more neurons over larger areas. The observation that stimulation as weak as 20 μA elicits responses hundreds of micrometers from the stimulation electrode indicates that action potentials in axons propagate throughout the slice, to elicit synaptic responses which have been shown to depend on glutamate receptor activation (Canales et al. 2022). Axons radiate out from the stimulation site so there is a lower density of activated axons at greater distances. This reduces the density of PV interneurons activated at greater distances by low current. Stronger currents activate more cells over a larger area. Response patterns varied but often included interlaminar and intralaminar responses across multiple layers and columns. These excitatory responses propagated away from the stimulating electrode and extended to the edges of the field of view within roughly 10 ms. The time course of this spread was used to measure conduction velocity.

Determination of conduction velocity

Following identification of barrel and layer boundaries in gradient contrast and fluorescence images (Fig. 3A–B), ROIs were delineated within the stimulated column (for interlaminar velocity) or within the stimulated layer (for intralaminar velocity) (Fig. 3C; see Materials and methods). Stimulus-induced fluorescence changes reported the roughly synchronous depolarization of PV interneurons within each ROI (Fig. 3E), and latency was measured as the

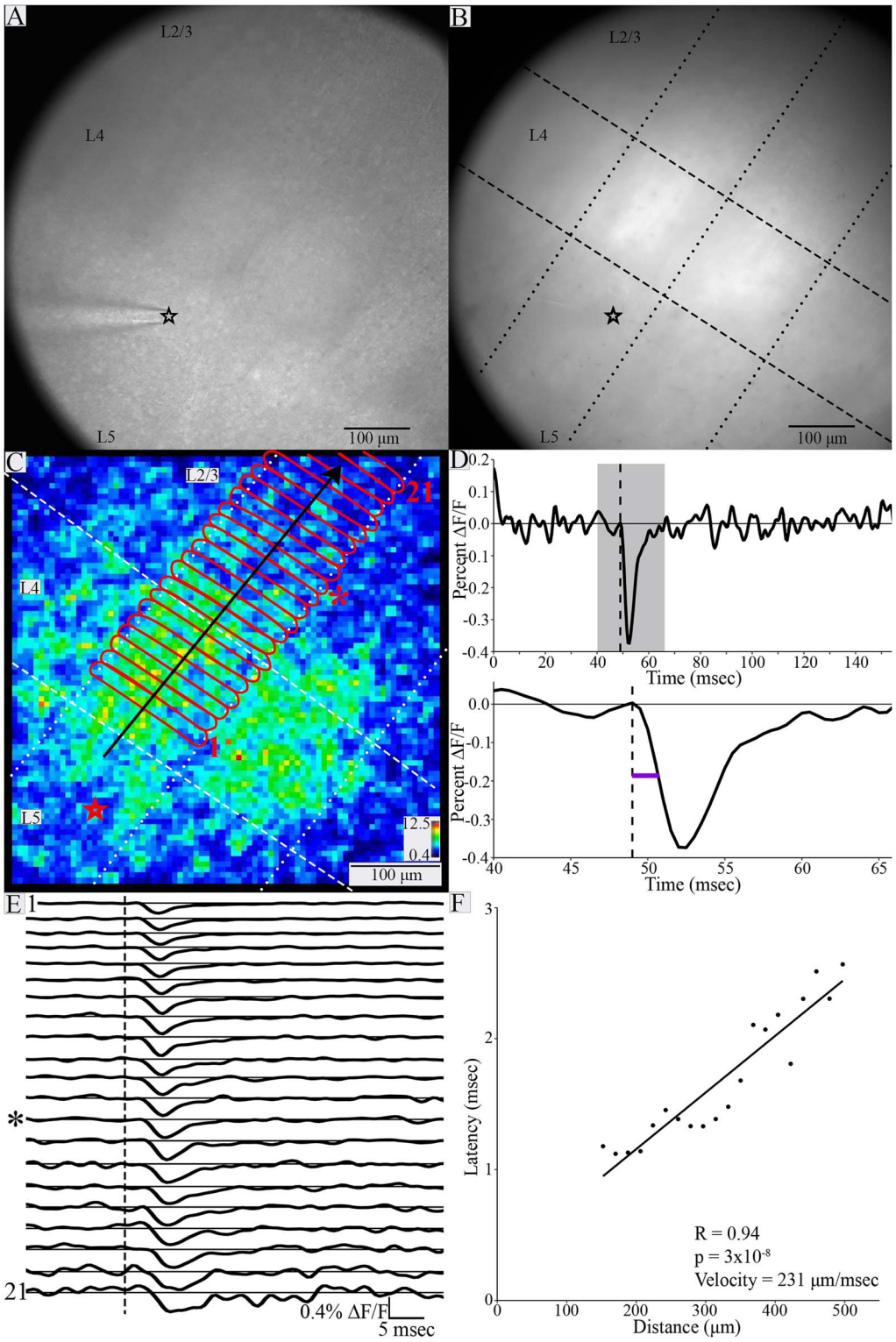

Fig. 3. Spread of PV interneuron responses and determination of conduction velocity. Gradient contrast image (A) and fluorescence image (B) of a BC slice (both taken with the high-resolution Kiralux camera) with stimulating electrode in L5 (black star at the tip). Layer boundaries and barrels are visible in L4 in A. In B, layer boundaries are indicated with dashed lines, and column boundaries with dotted lines (in C as well). (C) Heatmap of response SNR from the slice shown in A and B. Stimulation site indicated by red star (position differs slightly from A and B due to different cameras). Red outlines define ROIs ~20 µm thick spanning the stimulated column. Black arrow indicates direction of propagation. (D) Top: Trace of fluorescence versus time for ROI indicated by asterisk in C and E. Gray shading indicates the 20 ms measurement window expanded below. Bottom: Latency (purple line) is the time from stimulation (dashed line) to half-maximal change in fluorescence of the rising phase. (E) Traces of fluorescence versus time for 21 ROIs in sequence from bottom up (increasing distance from stimulation electrode). ROI 1 was closest to the electrode, and ROI 21 was farthest from the electrode. ROIs 1, 13 (star), and 21 are labeled in C. Dashed line indicates stimulation time, and asterisk indicates trace corresponding to the ROI marked with asterisk in C (thirteenth from bottom). Traces show PV interneuron responses with advancing latency. Higher noise in darker regions closer to the edge of the slice reduces SNR (e.g. ROI 21). (F) Latency plotted versus distance from the site of stimulation. The relationship between latency and distance was significant ($R = 0.94$, $P = 3 \times 10^{-8}$). The inverse of the slope gave an interlaminar conduction velocity of 231 µm/ms.

time from stimulation to half-maximal change in fluorescence (Fig. 3D). As stated in Materials and methods, plots of latency versus distance were fitted by linear regression and the conduction velocity was taken as the inverse of the slope (Fig. 3F). Despite showing PV interneuron response propagation, 15 plots of latency versus distance were not significantly correlated. In seven of these 15 plots, estimated conduction velocity was faster than the highest velocity obtained from plots showing significant correlations. In these cases, the spread within the field of view may have been too fast to detect differences in latency, as latencies in these plots varied by only 0.65 ± 0.16 ms (mean ± SD), and the average root-mean-square error in latency in this plot was 0.18 ms. The lack of significant correlation between latency and distance in the other 8 cases with slower apparent propagation reflects higher measurement error in these experiments. Examples of these two kinds of plots and a breakdown are shown in Fig. S2 of Supplementary Material. The analysis presented here is based entirely on conduction velocity measurements with significant distance-latency correlations and we recognize that this biases our analysis uniformly toward slower conduction.

Interlaminar and intralaminar conduction velocity

We next assessed conduction velocity for different propagation trajectories. Inter- and intralaminar conduction velocities were determined for stimulation in L2/3, L4, or L5. For the velocity of L2/3 → L5 conduction, we identified slices with clear propagation of PV interneuron responses within the stimulated column. Of five slices with seven or more ROIs containing responses, two had significant correlations between latency and distance. In both slices, responses spanned L2/3 → L5, and their conduction velocities were 360 and 372 μm/ms. Figure 4A displays three sequential SNR heatmaps at 1 ms intervals. Note that these are snapshots at specific times rather than peak SNR heatmaps as in Figs. 1–3. This sequence of snapshots illustrates L2/3 → L5 conduction and Fig. 4B displays the associated plot of latency versus distance, yielding a velocity for this experiment of 360 μm/ms.

For interlaminar responses to L4 stimulation, three of six slices yielded plots with significant correlations. The velocity of L4 → L2/3 interlaminar conduction was 223 ± 87 μm/ms (mean ± SD, $N = 2$, example in Fig. 4C and D), and for the one experiment with L4 → L5 interlaminar conduction the velocity was 414 μm/ms. Overall, combined L4 → L2/3 and L4 → L5 conduction velocity was 286 ± 127 μm/ms (mean ± SD, $N = 3$).

In response to L5 stimulation, 16 of 18 slices produced significant correlations, and responses spread to L2/3 in all cases. L5 → L2/3 conduction velocity was 296 ± 122 μm/ms (mean ± SD, $N = 16$, example in Fig. 4E and F). The greater number of interlaminar velocity measurements compared to other trajectories was primarily due to less interference from disynaptic responses (Fig. S2, Supplementary Material).

Of the nine slices showing L2/3 intralaminar conduction, latency, and distance were significantly correlated in six, yielding a conduction velocity of 200 ± 93 μm/ms (mean ± SD, $N = 6$). Responses were restricted to the stimulated and immediately adjacent columns (Fig. 5A and B) in all but one slice. In that slice responses extended to one additional column. Of 6 slices exhibiting L4 intralaminar conduction, latency, and distance were significantly correlated in four, yielding a conduction velocity of 142 ± 76 μm/ms (mean ± SD, $n = 4$). Responsive ROIs spanned the home and neighboring columns in two slices (Fig. 5C and D) and extended to an additional adjacent column in two more slices. Finally, in the two slices exhibiting L5 intralaminar conduction, the latency-distance plots were uncorrelated and no velocity was determined.

Combining measurements in 21 slices from 11 animals, average interlaminar conduction velocity to stimulation in L2/3, L4, and L5 was 302 ± 115 μm/ms (mean ± SD). L2/3 and L4 intralaminar conduction velocity in 10 slices from seven animals was 177 ± 87 μm/ms (mean ± SD). Interlaminar conduction velocity was therefore ∼71% faster than intralaminar conduction velocity (Fig. 6A), and this difference was significant [$t(22.996) = 3.344$, $P = 0.003$, Welch's two-sample t-test]. L4 → L2/3 or L5 and L5 → L2/3 conduction velocities were not significantly different [$t(2.740) = -0.124$, $P = 0.910$, Welch's two-sample t-test, Fig. 6B]. L2/3 and L4 intralaminar conduction velocities also were not significantly different [$t(7.506) = 1.086$, $P = 0.311$, Welch's two-sample t-test, Fig. 6B]. In one slice exhibiting both interlaminar and intralaminar conduction, both velocities could be measured. In this slice, L4 → L5 conduction (414 μm/ms) was more than twice as fast as intralaminar L4 conduction (159 μm/ms), in keeping with the trend of more rapid interlaminar conduction. In summary, we measured conduction velocity of excitatory axons targeting PV interneurons across multiple trajectories, and found that interlaminar conduction within columns is significantly faster than intralaminar conduction between columns.

Discussion

This study used voltage imaging from PV interneurons to investigate propagation through interlaminar and intralaminar circuits in the BC. Response patterns recapitulated circuitry across known pathways. Canonically, thalamic input enters the cortex through L4, and L4 then drives L2/3 PV interneurons (Helmstaedter et al. 2008; Xu and Callaway 2009; Adesnik et al. 2012; Staiger and Petersen 2021). We determined L4 → L2/3 conduction velocity to be 223 ± 87 μm/ms. While both basket cells and chandelier cells are present in L2/3, L4 neurons do not target L2/3 chandelier cells (Xu and Callaway 2009). This velocity therefore reflects conduction along axons specifically targeting L2/3 basket cells. In addition to the canonical L4 → L2/3 path, spiny stellate cells in L4 project to PV interneurons in L5 (Pluta et al. 2015). We determined L4 → L5 conduction velocity to be 414 μm/ms based on one slice, and it was faster than both L4 → L2/3 conduction velocities (161 and 284 μm/msec). Continuing along the canonical circuit, L2/3 pyramidal cells project to L5 excitatory and inhibitory cells, including PV interneurons (Lourenco et al. 2020). Stimulating L2/3 excited PV interneurons in both L4 and L5. With velocities of 360 and 372 μm/ms, L2/3 → L5 conduction was the fastest found in the present study. Finally, L5 conduction to L4 and L2/3 had a velocity of 296 ± 122 μm/ms. L2/3 chandelier cells receive especially strong input from L5A (Xu and Callaway 2009). Because we stimulated mainly in the upper portion of L5, this velocity may reflect this projection. Overall, the basic patterns of spread we see recapitulate the known functional connectivity between cortical layers in BC, and our work provides velocities for conduction along these projections.

Our findings are also consistent with intralaminar connectivity in BC. L2/3 pyramidal cell axons extend horizontally into neighboring columns (Narayanan et al. 2015), and stimulating L2/3 in rat somatosensory cortex can elicit intralaminar responses up to 2 mm away (Telfeian and Connors 2003). L4 spiny stellate cell axons also sometimes cross into a neighboring barrel (Egger et al. 2008; Staiger and Petersen 2021). We report L2/3 (200 ± 93 μm/ms) and L4 (142 ± 76 μm/ms) intralaminar conduction velocity through these circuits. Intralaminar PV

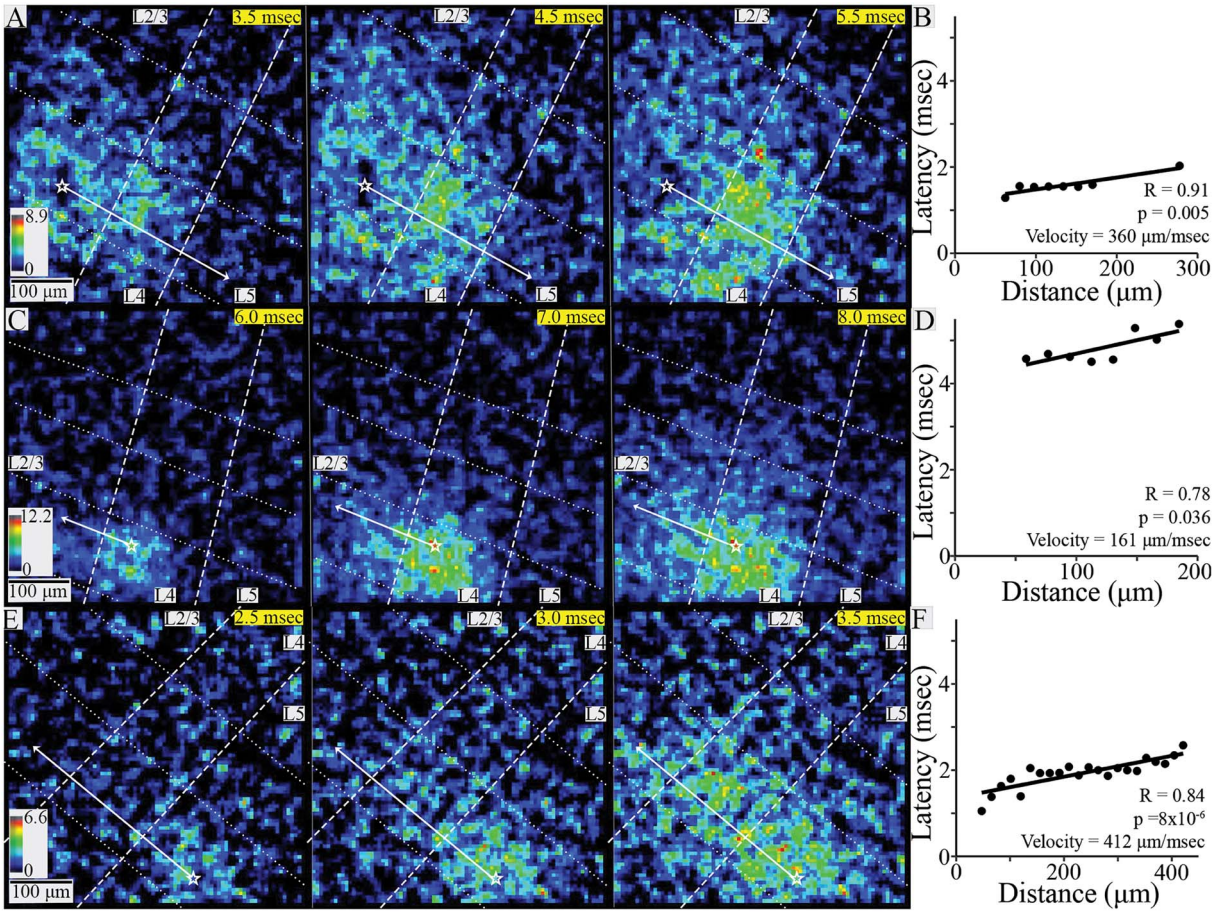

Fig. 4. Interlaminar conduction. (A) SNR heatmaps at 1-ms intervals showing the spread of PV interneuron responses to stimulation in L2/3. (B) Latency versus distance within the stimulated column in the slice shown in A ($R = 0.91$, $P = 0.005$) yielded a conduction velocity of 360 µm/ms. (C) SNR heatmaps at 1-ms intervals showing PV interneuron responses to stimulation in L4. (D) Latency versus distance within the stimulated column in the slice shown in C ($R = 0.78$, $P = 0.036$) yielded a conduction velocity of 161 µm/ms. (E) SNR heatmaps at 0.5-ms intervals showing PV interneurons responses to stimulation in L5. (F) Latency versus distance within the stimulated column in the slice shown in E ($R = 0.84$, $P = 8 \times 10^{-6}$) yielded a conduction velocity of 412 µm/ms. In all SNR heatmaps, white stars mark stimulation site and solid white arrows show propagation trajectories used for velocity determination; dashed lines show layer boundaries, and dotted lines show column boundaries. Time after stimulation is shown in the upper right corner of each heatmap on yellow background.

interneuron responses remained within the stimulated column and a neighboring column in seven experiments but spread to an additional column in three experiments. This supports the concept of transcolumnar axons emerging from an "intracortical unit" spanning three-barrel columns (Narayanan et al. 2015). Although L5 axons can extend intralaminarly through up to two neighboring columns, we observed intralaminar L5 conduction in only two slices and were unable to measure the velocities. We were able to image conduction along previously described interlaminar and L2/3 and L4 intralaminar circuits within BC, and again provided velocities of propagation along these trajectories.

Our conduction velocity range from 74 to 473 µm/ms is broadly consistent with previous measurements in murine hippocampus and cortex determined by various methods, including antidromic activation (300 µm/ms, Shlosberg et al. 2008), microelectrode arrays (330 µm/ms, Bakker et al. 2009), patch clamp recording (363 µm/ms, Salami et al. 2003; 150–550 µm/ms, Murakoshi et al. 1993; 400 µm/ms, Telfeian and Connors 2003; 200 µm/ms, Helmstaedter et al. 2008), voltage sensitive dye (50–450 µm/ms, Popovic et al. 2011), and axon-targeted hVOS (94 and 228 µm/ms, Ma et al. 2017). We report that interlaminar conduction (302 ± 115 µm/ms) is 71% faster than intralaminar conduction (177 ± 87 µm/ms). Because functions differ for interlaminar and intralaminar circuits, these differences likely have functional implications. L4 → L2/3 conduction impacts integration of intracortical and thalamic input in L2/3 (Staiger and Petersen 2021). Optogenetic inhibition of L4 excitatory cells broadens L5 sensory tuning curves by increasing responses to nonpreferred stimuli, and this effect is likely mediated by L5 PV interneurons (Pluta et al. 2015). Stress decreases PV interneuron activity across L2-L5, reduces dendritic spines on L5 pyramidal cells, and impairs texture discrimination. Stimulation of PV interneurons ameliorates these deficits (Chen et al. 2018). Finally, PV interneurons are hypothesized to decrease synchrony between L4 and L5 during active sensory periods (Jang et al. 2020), and small changes in conduction velocity can have large impacts on synchrony (Pajevic et al. 2014; Ivanov et al. 2019).

Timing of intralaminar input to PV interneurons from neighboring columns likely plays a role in multi-whisker integration. In visual cortex both pyramidal cells and inhibitory interneurons show directional preference (Andermann and Moore 2006), and L2/3 intralaminar axons might connect regions with similar preferred directions (Gilbert 1992). L3 and L4 neurons in columns corresponding to whiskers along the same arc have

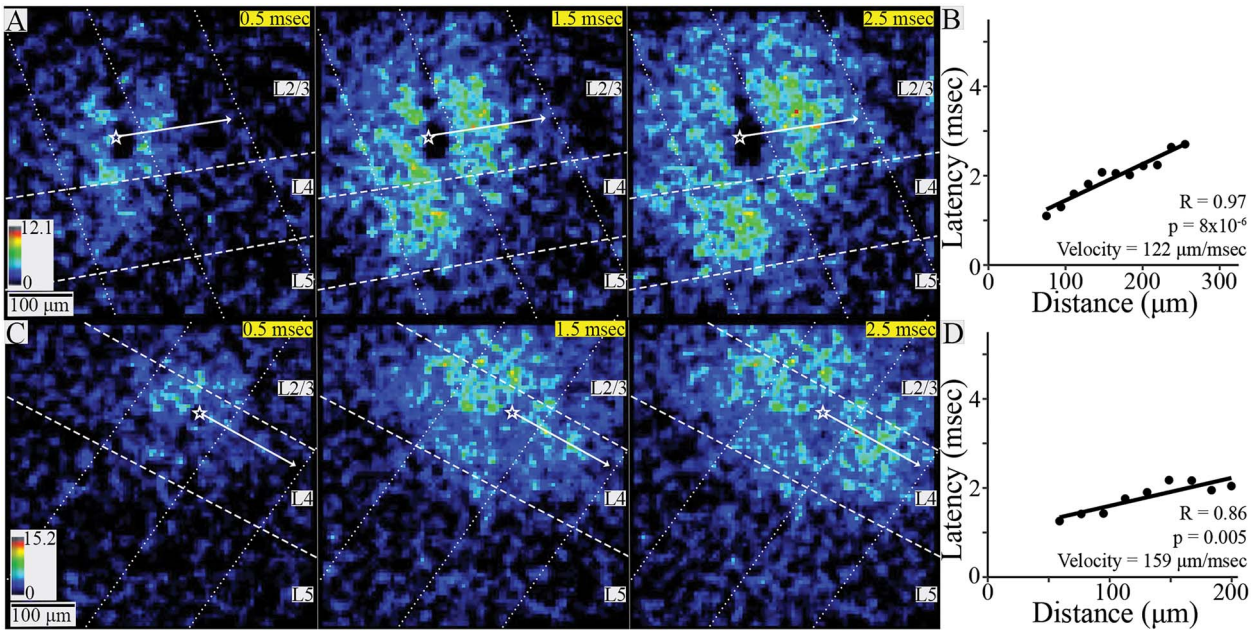

Fig. 5. Intralaminar conduction. (A) SNR heatmaps at 1-ms intervals showing the spread of PV interneuron responses within L2/3 to stimulation in that layer. Responses spread within the stimulated column and to a neighboring column. (B) Latency versus distance for the slice shown in A ($R = 0.97$, $P = 8 \times 10^{-6}$) yielded a conduction velocity of 112 μm/ms. (C) SNR heatmaps at 1-ms intervals showing PV interneuron responses within L4 to stimulation in that layer. (D) Latency versus distance for the slice shown in C ($R = 0.86$, $P = 0.005$) yielded a conduction velocity of 159 μm/ms. In all heatmaps, white stars mark stimulation site and white arrows show PV interneuron response propagation trajectories; dashed lines show layer boundaries, and dotted lines show column boundaries. Time after stimulation shown in upper right corner of each heatmap on yellow background.

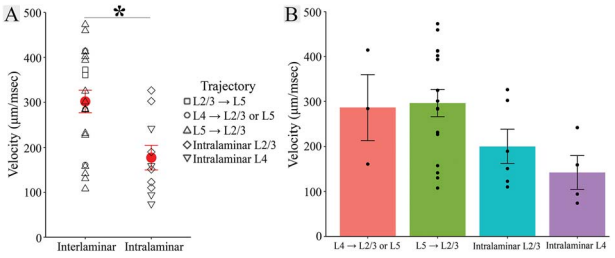

Fig. 6. Interlaminar and intralaminar conduction velocity. (A) Interlaminar velocity (302 ± 115 μm/ms, 21 slices) was ~71% faster than intralaminar velocity [177 ± 87 μm/ms, 10 slices; t(22.996) = 3.344, $P = 0.003$, Welch's two-sample *t*-test]. Symbol shapes indicate velocity trajectory (in legend), and group mean ± SE are shown in red. (B) L4 → L2/3 or L5 (286 ± 127 μm/ms, three slices), L5 → L2/3 (296 ± 122 μm/ms, 16 slices), L2/3 intralaminar (200 ± 93 μm/ms, six slices) and L4 intralaminar (142 ± 76 μm/ms, four slices) velocity. Error bars indicate SE.

similar preferred whisker stimulation frequencies (Andermann et al. 2004), and L2/3 excitation spreads across columns related to whiskers along rows *before* arcs (Petersen et al. 2003). L2/3 and L4 intralaminar conduction velocity may therefore impact multi-whisker integration of frequency and direction preferences differentially. Our finding that interlaminar conduction is faster than intralaminar conduction will make computations within a barrel column faster than across columns. Thus, multi-whisker integration, which depends on intralaminar communication between barrel columns, will occur more slowly than computations within columns related to intracortical synchrony, sensory tuning, and texture discrimination.

hVOS imaging offers a powerful approach to the study of conduction velocity, not only in the axons of defined cell types (Ma et al. 2017), but also in the axons defined by their targets. Although DPA increases membrane capacitance and thus slows propagation, this effect is small as increasing DPA from 2 to 4 μM reduced conduction velocity by only 15% in mossy fibers (Ma et al. 2017). Furthermore, this nonspecific effect should reduce conduction velocity proportionally in different populations of axons. Voltage imaging has historically provided a powerful method for the measurement of axonal conduction velocity (Grinvald et al. 1981; Sakai et al. 1991; Popovic et al. 2011; Hamada et al. 2017), and genetically encoded voltage indicators have extended this approach (Ma et al. 2019; Panzera and Hoppa 2019). Targeting hVOS probes to different types of neurons thus has the potential to reveal additional axonal specializations adapted to different forms of neuronal computation.

Supplementary material

Supplementary material is available at *Cerebral Cortex* Journal online.

Acknowledgments

This work was supported by National Institutes of Health (NS127219 and NS093866 to MBJ; NS105200 to XZ; and T32GM13-0550 to JJ). We thank Dr Shane McMahon for methodological contributions.

Conflict of interest statement: None declared.

Author contributions

Katherine S. Scheuer (Conceptualization, Data curation, Formal analysis, Investigation, Methodology, Software, Validation, Visualization, Writing—original draft, Writing—review & editing), John Judge (Data curation, Formal analysis, Software, Writing—review

& editing), Xinyu Zhao (Funding acquisition, Resources, Writing—review & editing), and Meyer B. Jackson (Conceptualization, Formal analysis, Funding acquisition, Supervision, Visualization, Writing—review & editing)

References

Adesnik H. Layer-specific excitation/inhibition balances during neuronal synchronization in the visual cortex. *J Physiol-London*. 2018:596:1639–1657.

Adesnik H, Bruns W, Taniguchi H, Huang ZJ, Scanziani M. A neural circuit for spatial summation in visual cortex. *Nature*. 2012:490: 226–231.

Allitt BJ, Alwis DS, Rajan R. Laminar-specific encoding of texture elements in rat barrel cortex. *J Physiol*. 2017:595:7223–7247.

Andermann ML, Moore CI. A somatotopic map of vibrissa motion direction within a barrel column. *Nat Neurosci*. 2006:9:543–551.

Andermann ML, Ritt J, Neimark MA, Moore CI. Neural correlates of vibrissa resonance: band-pass and somatotopic representation of high-frequency stimuli. *Neuron*. 2004:42:451–463.

Ayaz A, Stauble A, Hamada M, Wulf MA, Saleem AB, Helmchen F. Layer-specific integration of locomotion and sensory information in mouse barrel cortex. *Nat Commun*. 2019:10:2585.

Bakker R, Schubert D, Levels K, Bezgin G, Bojak I, Kotter R. Classification of cortical microcircuits based on micro-electrode-array data from slices of rat barrel cortex. *Neural Netw*. 2009:22: 1159–1168.

Bayguinov PO, Ma YH, Gao Y, Zhao XY, Jackson MB. Imaging voltage in genetically defined neuronal subpopulations with a cre recombinase-targeted hybrid voltage sensor. *J Neurosci*. 2017:37: 9305–9319.

Bradley J, Luo R, Otis TS, DiGregorio DA. Submillisecond optical reporting of membrane potential in situ using a neuronal tracer dye. *J Neurosci*. 2009:29:9197–9209.

Canales A, Scheuer KS, Zhao X, Jackson MB. Unitary synaptic responses of parvalbumin interneurons evoked by excitatory neurons in the mouse barrel cortex. *Cereb Cortex*. 2022:33(9): 5108–5121.

Cardin JA. Inhibitory interneurons regulate temporal precision and correlations in cortical circuits. *Trends Neurosci*. 2018:41(10): 689–700.

Chanda B, Blunck R, Faria LC, Schweizer FE, Mody I, Bezanilla F. A hybrid approach to measuring electrical activity in genetically specified neurons. *Nat Neurosci*. 2005:8:1619–1626.

Chang PY. *Heterogeneous spatial patterns of long-term potentiation in hippocampal slices*. Madison, WI: University of Wisconsin-Madison; 2006 p. 144

Chen CC, Lu J, Yang R, Ding JB, Zuo Y. Selective activation of parvalbumin interneurons prevents stress-induced synapse loss and perceptual defects. *Mol Psychiatry*. 2018:23:1614–1625.

Egger V, Nevian T, Bruno RM. Subcolumnar dendritic and axonal organization of spiny stellate and star pyramid neurons within a barrel in rat somatosensory cortex. *Cereb Cortex*. 2008:18:876–889.

Feldmeyer D. Excitatory neuronal connectivity in the barrel cortex. *Front Neuroanat*. 2012:6:24.

Ferguson BR, Gao WJ. PV interneurons: critical regulators of E/I balance for prefrontal cortex-dependent behavior and psychiatric disorders. *Front Neural Circuits*. 2018:12:37.

Galarreta M, Hestrin S. Electrical and chemical synapses among parvalbumin fast-spiking GABAergic interneurons in adult mouse neocortex. *Proc Natl Acad Sci USA*. 2002:99:12438–12443.

Ghitani N, Bayguinov PO, Ma YH, Jackson MB. Single-trial imaging of spikes and synaptic potentials in single neurons in brain slices with genetically encoded hybrid voltage sensor. *J Neurophysiol*. 2015:113:1249–1259.

Gilbert CD. Horizontal integration and cortical dynamics. *Neuron*. 1992:9:1–13.

Gonzalez-Burgos G, Cho RY, Lewis DA. Alterations in cortical network oscillations and parvalbumin neurons in schizophrenia. *Biol Psychiatry*. 2015:77:1031–1040.

Grinvald A, Ross WN, Farber I. Simultaneous optical measurements of electrical activity from multiple sites on processes of cultured neurons. *Proc Natl Acad Sci USA*. 1981:78:3245–3249.

Hamada MS, Popovic MA, Kole MH. Loss of saltation and presynaptic action potential failure in demyelinated axons. *Front Cell Neurosci*. 2017:11:45.

Helmstaedter M, Staiger JF, Sakmann B, Feldmeyer D. Efficient recruitment of layer 2/3 interneurons by layer 4 input in single columns of rat somatosensory cortex. *J Neurosci*. 2008:28: 8273–8284.

Isett BR, Feasel SH, Lane MA, Feldman DE. Slip-based coding of local shape and texture in mouse S1. *Neuron*. 2018:97:418, e415–433.

Ivanov VA, Polykretis IE, Michmizos KP. 2019. Axonal conduction velocity impacts neuronal network oscillations. *2019 IEEE Embs International Conference on Biomedical & Health Informatics (Bhi)*. IEEE Institute of Electrical and Electronics Engineers, Piscataway, Ne Jersey.

Jang HJ, Chung HW, Rowland JM, Richards BA, Kohl MM, Kwag JY. Distinct roles of parvalbumin and somatostatin interneurons in gating the synchronization of spike times in the neocortex. *Sci Adv*. 2020:6(17):eaay5333.

Lauber E, Filice F, Schwaller B. Parvalbumin neurons as a hub in autism spectrum disorders. *J Neurosci Res*. 2018:96:360–361.

Lefort S, Tomm C, Floyd Sarria JC, Petersen CC. The excitatory neuronal network of the C2 barrel column in mouse primary somatosensory cortex. *Neuron*. 2009:61:301–316.

Lenschow C, Brecht M. Barrel cortex membrane potential dynamics in social touch. *Neuron*. 2015:85:718–725.

Liu TY, Hsieh JC, Chen YS, Tu PC, Su TP, Chen LF. Different patterns of abnormal gamma oscillatory activity in unipolar and bipolar disorder patients during an implicit emotion task. *Neuropsychologia*. 2012:50:1514–1520.

Lourenco J, De Stasi AM, Deleuze C, Bigot M, Pazienti A, Aguirre A, Giugliano M, Ostojic S, Bacci A. Modulation of coordinated activity across cortical layers by plasticity of inhibitory synapses. *Cell Rep*. 2020:30:630, e635–641.

Ma Y, Bayguinov PO, Jackson MB. Action potential dynamics in fine axons probed with an Axonally targeted optical voltage sensor. *ENEURO*. 2017:4(4):0146–0117.

Ma YH, Bayguinov PO, Jackson MB. Optical studies of action potential dynamics with hVOS probes. *Curr Opin Biomed Eng*. 2019:12: 51–58.

Murakoshi T, Guo JZ, Ichinose T. Electrophysiological identification of horizontal synaptic connections in rat visual cortex in vitro. *Neurosci Lett*. 1993:163:211–214.

Narayanan RT, Egger R, Johnson AS, Mansvelder HD, Sakmann B, de Kock CP, Oberlaender M. Beyond columnar organization: cell type- and target layer-specific principles of horizontal axon projection patterns in rat Vibrissal cortex. *Cereb Cortex*. 2015:25: 4450–4468.

O'Connor DH, Peron SP, Huber D, Svoboda K. Neural activity in barrel cortex underlying vibrissa-based object localization in mice. *Neuron*. 2010:67:1048–1061.

Pajevic S, Basser PJ, Fields RD. Role of myelin plasticity in oscillations and synchrony of neuronal activity. *Neuroscience*. 2014:276: 135–147.

Panzera LC, Hoppa MB. Genetically encoded voltage indicators are illuminating subcellular physiology of the axon. *Front Cell Neurosci*. 2019:13:52.

Petersen CC, Grinvald A, Sakmann B. Spatiotemporal dynamics of sensory responses in layer 2/3 of rat barrel cortex measured in vivo by voltage-sensitive dye imaging combined with whole-cell voltage recordings and neuron reconstructions. *J Neurosci*. 2003:23:1298–1309.

Pluta S, Naka A, Veit J, Telian G, Yao L, Hakim R, Taylor D, Adesnik H. A direct translaminar inhibitory circuit tunes cortical output. *Nat Neurosci*. 2015:18:1631–1640.

Popovic MA, Foust AJ, McCormick DA, Zecevic D. The spatio-temporal characteristics of action potential initiation in layer 5 pyramidal neurons: a voltage imaging study. *J Physiol*. 2011:589:4167–4187.

Pouille F, Scanziani M. Enforcement of temporal fidelity in pyramidal cells by somatic feed-forward inhibition. *Science*. 2001:293:1159–1163.

Sakai T, Komuro H, Katoh Y, Sasaki H, Momose-Sato Y, Kamino K. Optical determination of impulse conduction velocity during development of embryonic chick cervical vagus nerve bundles. *J Physiol*. 1991:439:361–381.

Salami M, Kimura F, Tsumoto T. Postnatal changes of conduction velocity of the fibers in and out of the mouse barrel cortex. *Iran Biomed J*. 2003:7(2):57–63.

Shlosberg D, Abu-Ghanem Y, Amitai Y. Comparative properties of excitatory and inhibitory inter-laminar neocortical axons. *Neuroscience*. 2008:155:366–373.

Staiger JF, Petersen CCH. Neuronal circuits in barrel cortex for whisker sensory perception. *Physiol Rev*. 2021:101:353–415.

Swadlow HA. Efferent neurons and suspected interneurons in S-1 forelimb representation of the awake rabbit: receptive fields and axonal properties. *J Neurophysiol*1990. 1990:63(6):1477–1498.

Swadlow HA. Efferent neurons and suspected interneurons in second somatosensory cortex of the awake rabbit: receptive fields and axonal properties. *J Neurophysiol*. 1991:66:1392–1409.

Telfeian AE, Connors BW. Widely integrative properties of layer 5 pyramidal cells support a role for processing of extralaminar synaptic inputs in rat neocortex. *Neurosci Lett*. 2003:343:121–124.

Vecchia D, Beltramo R, Vallone F, Chereau R, Forli A, Molano-Mazon M, Bawa T, Binini N, Moretti C, Holtmaat A, et al. Temporal sharpening of sensory responses by layer V in the mouse primary somatosensory cortex. *Curr Biol*. 2020:30:1589, e1510–1599.

Wang D, Zhang Z, Chanda B, Jackson MB. Improved probes for hybrid voltage sensor imaging. *Biophys J*. 2010:99:2355–2365.

Woolsey TA, Van der Loos H. The structural organization of layer IV in the somatosensory region (S1) of mouse cerebral cortex. *Brain Res*. 1970:17:20542.

Xu X, Callaway EM. Laminar specificity of functional input to distinct types of inhibitory cortical neurons. *J Neurosci*. 2009:29:70–85.

Xu XM, Olivas ND, Ikrar T, Peng T, Holmes TC, Nie Q, Shi YL. Primary visual cortex shows laminar-specific and balanced circuit organization of excitatory and inhibitory synaptic connectivity. *J Physiol-London*. 2016:594:1891–1910.

Yeganeh F, Knauer B, Guimaraes Backhaus R, Yang JW, Stroh A, Luhmann HJ, Stuttgen MC. Effects of optogenetic inhibition of a small fraction of parvalbumin-positive interneurons on the representation of sensory stimuli in mouse barrel cortex. *Sci Rep*. 2022:12:19419.